Machine Learning-Enhanced Combustion Modelling: Predicting Ethanol Effects in a Single-Cylinder Research Engine

Published Version:
Ferrari, L., Sammito, G., Fischer, M., Cavina, N. (2025). Machine Learning-Enhanced Combustion Modelling: Predicting Ethanol Effects in a Single-Cylinder Research Engine. Warrendale, Pennsylvania : SAE International [10.4271/2025-24-0026].

Availability:
This version is available at: https://hdl.handle.net/11585/1033743 since: 2026-02-20

Published:

DOI: http://doi.org/10.4271/2025-24-0026

Machine Learning-Enhanced Combustion Modelling: Predicting Ethanol Effects in a Single-Cylinder Research Engine

Author, co-author (Do NOT enter this information. It will be pulled from participant tab in MyTechZone)

Affiliation (Do NOT enter this information. It will be pulled from participant tab in MyTechZone)

Abstract

Recent studies highlight the urgent need to reduce greenhouse gas (GHG) emissions to mitigate the impacts of global warming and climate change. As a major contributor, the transport sector plays a vital role in these efforts. Ethanol emerges as a promising fuel for decarbonising hard-to-electrify propulsion sectors, thanks to its sustainable production pathways and favourable physical and combustion properties, such as energy density, rapid burning velocity, and high knock resistance. This work proposes a methodology to enable the possibility of replicating the combustion behaviour of ethanol in a 1D CFD simulation environment representative of a single-cylinder research engine. Spark-ignition combustion is simulated through the Eddy Burn-Up combustion model previously calibrated for standard fossil gasoline. The combustion model features a laminar flame speed neural network, trained and tested through reference chemical kinetics simulations. The combustion model showed great accuracy in replicating key combustion metrics, highlighting its predictive capability while switching fuel kinds. Eventually, knock occurrence was evaluated by employing the Livengood-Wu induction time integral. The model was adjusted by the induction integral multiplier to align the knock predictions to the normalised experimental Mean Amplitude Pressure Oscillation value. The latest remains always below 1, meaning that the engine can be run at maximum combustion efficiency without knock occurrence even at maximum load.

Introduction

Between 2011 and 2020, the mean global temperature was recorded to be 1.09°C higher than during the period from 1850 to 1900 [1]. This increase in the average global temperature is commonly referred to as global warming. Global warming is responsible for a range of adverse phenomena, including rising sea levels, glacier melting, shifts in precipitation patterns, alterations in the frequency of extreme weather events (such as flash floods and heat waves), fluctuations in crop yields, and heightened water and food insecurity. The term climate change is commonly used to encompass all these phenomena, which collectively pose a significant threat to human society [2]. Global warming is primarily driven by the accumulation of greenhouse gases (GHG$_s$) in the Earth's atmosphere, and among them, CO_2 has by far the largest impact on the greenhouse effect, accounting for approximately 64% of the overall infrared radiation absorption and re-emission [2].

The use of alternative sustainable fuels enables tackling GHG emissions from another perspective. Although renewable fuels are more expensive than their fossil counterpart, they offer a great potential to reduce not only carbon dioxide emissions but also regulated and unregulated emissions [3], [4], [5]. Other than drop-in solutions, meaning that such fuels can be used in modern internal combustion engines without major modifications, Flex-Fuel Vehicles (FFV) allow the use of non-drop-in renewable fuels in high concentrations, such as ethanol, up to 85 % (E85) or even 100 % (E100). Practically, the Engine Management System (EMS) of FFV$_s$, gets the signal from the lambda and the ethanol concentration sensors, and it adjusts the engine operating parameters like boost pressure, injection timing and quantity, ignition timing, and the Exhaust Gas Recirculation (EGR) system [6]. Specifically, the ignition timing is advanced to get to maximum brake torque (MBT) without knocking for increasing ethanol content in gasoline, complying with the optimum 50% mass fraction burned (MFB), within the range of 8 to 10 ° after top dead centre, or the maximum exhaust gas temperature of 900°C at MBT conditions [7]. In addition, the injection timing and duration are calibrated to minimise the cycle-to-cycle variations and to account for the lower stoichiometric air-to-fuel ratio as the ethanol content increases [6]. Such a strategy enables using ethanol more efficiently compared to regular gasoline-calibrated SI engines [8].

Among all the renewable energy sources capable of reducing greenhouse gas emissions, bioethanol is one of the most used bio-fuels for transportation [9], [10]. Bioethanol could be employed both in Spark-Ignited (SI) engines and Compression Ignited (CI) ones. In the first case, ethanol can replace different percentages of mineral gasoline in fuel blends, from small volumetric fractions up to complete replacement of the traditional petrol [11]. Instead, in diesel engines, bioethanol is blended in small percentages, with the main objective of reducing emissions and particulate matter during the combustion process [12]. To minimise harmful emissions, ethanol has gained considerable importance over recent years [13], [14], [15]. Some studies also evaluated the possibility of using ethanol in dual-fuel mode with gaseous fuels, like natural gas and biogas [16], [17]. The studies reported that ethanol accelerates the combustion rate of the mixture, and improves knock resistance and thermal efficiency while reducing, at the same time, fuel consumption and pollutant emissions. In diesel engines, ethanol dual-fuel operation has shown the potential to reduce NO_x emissions and soot, without the need for expensive aftertreatment technology [18], [19], [20].

Table 1 reports a comparison between the characteristics of ethanol and those of standard RON95E10.

Property	**Ethanol**	**RON95E10**
C-content [% m/m]	52.36	82.77
H-content [% m/m]	13.11	13.71
O-content [% m/m]	34.53	3.53
Density @ 15°C [kg/m^3]	794.10	746.4
Lower heating value [MJ/kg]	26.87	41.59
Molar mass [g/mol]	46.33	87.7
RON/MON [-]	109/90	96.7/85.5
Vapour pressure DVPE [kPa]	15.60	58.8
Heat of vaporisation [kJ/kg]	923	420
C/H/O mass share [-]	2/6/1	6.05/11.93/0.19
Air-to-fuel ratio [-]	9	14.08
Aromatics [% V/V]	0	26.3
Olefines [% V/V]	0	9.4
Saturated hydrocarbons [% V/V]	0	54.7
Alcohols [% V/V]	100.00	9.5

Table 1. Investigated fuel properties

Ethanol shows a higher octane ratio than gasoline; therefore, higher compression ratios and combustion efficiency can be achieved without knock occurrence [21], [22], [23]. Another upside is its cooling capacity on the air-fuel mixture thanks to its heat of vaporisation, which further improves knock resistance, potentially fuel economy and volumetric efficiency [24]. One main drawback of using ethanol is its low vapour pressure, which poses challenges in cold start phases [25], [26]. When it comes to performance, due to the reduced lower heating value (LHV) and the poor mixture preparation of ethanol blends, the output brake torque is reduced at low engine speeds, instead, at higher rotational speeds the faster-burning capability of ethanol causes higher brake mean effective pressure (BMEP), brake torque and brake power [27], [28], [29]. Additionally, to produce the same amount of power, more fuel needs to be injected into the cylinder, causing the specific fuel consumption of ethanol blends and neat ethanol to grow on the back of the reduced ethanol LHV and stoichiometric air-to-fuel ratio [30]. This injected surplus ethanol fuel occupies a larger volume to keep the stoichiometric air-to-fuel ratio, which might result in a poor volumetric efficiency if the injection timing is not properly adjusted [31]. As for the emission characteristics, the unburnt hydrocarbons (HC) and carbon monoxide (CO) show a decreasing trend by adding ethanol at different proportions, thanks to the increment in the oxygen content and fuel oxidation quality, while the opposite trend is found for carbon dioxide (CO_2) emission. However, the difference in HC and CO emissions for ethanol blends and gasoline is minimal at lower speeds and loads due to the poor quality of the air-fuel mixture [32]. Additionally, the nitrogen oxide (NO_x) emissions can be reduced by adding ethanol, thanks to its enhanced evaporative cooling effect [33].

When it comes to materials employed for the internal combustion engine and the fuel supply system, ethanol poses some challenges. Special alloys are required for the cylinder liners, pistons, and piston rings to withstand high combustion temperatures and pressure [34]. Moreover, an anti-corrosive coating may be utilised in the fuel supply system and engine components due to the ethanol's highly corrosive nature [6]. A specific catalytic converter, wash coat, and recalibrated canister for higher purge flow may be necessary for FFV_s with ethanol blends. Furthermore, an auxiliary cold start system or ethanol heating system is required to overcome the cold start drivability issues and evaporative emissions caused by the lower vapour pressure of ethanol [35].

In this study, a novel methodology related to the prediction of ethanol combustion behaviour is presented. Starting from a one-dimensional (1D) CFD model, representative of a single-cylinder research engine employed for experimental data collection, whose combustion model was previously calibrated for standard fossil gasoline, neat ethanol combustion is simulated and predicted without the need for recalibrating the combustion model. Specifically, the Eddy Burn Up combustion model ([36], [37]) is adjusted only by leveraging the laminar flame speed (LFS) dataset, which is embedded into the combustion model via a neural network, rather than using the widely employed LFS correlations of Metghalchi et. al [38] and Gulder [39]. For validation purposes, experimental data were collected at the engine test bench, and they were provided by FEV GmbH.

This work is organised as follows: Section 1 presents the experimental setup used for the data gathering, while Section 2 presents the outcomes from the three-pressure analysis (TPA) employed to validate the experimental data. Section 3 highlights the methodology followed to simulate the laminar flame speeds and ignition delays of the fuel under analysis. Moreover, the results of the predictive combustion model and the knock prediction model will be shown as well.

Experimental setup

The experimental data for this study were provided by FEV Group GmbH. A single-cylinder research engine (SCRE) was utilised for data acquisition, and the main engine characteristics are reported in Table 2.

Engine type	Single-cylinder, 4-stroke
Piston	Flat
Combustion chamber	Hemispherical
Displaced volume	500 cc
Stroke x Bore	113.2 x 75 mm
Stroke/Bore ratio	1.51
Connecting rod length	220 mm
Crank radius	56.6 mm
Compression ratio	Adjustable, (10.8:1, 12.2:1, 15:1)
Number of valves	4

Injection type	Direct
Valve timing	Variable
Max. peak cylinder pressure	180 bar
Max. fuel pressure	200 bar
Fuel injector	6-hole solenoid

Table 2. HELEN engine hardware specifications

The selected compression ratio (CR) for this analysis was 10.8:1 since the combustion model was previously calibrated for standard fossil gasoline according to this CR. Moreover, the engine could be operated with a variable valve timing (VVT) system. For fuel injection, a centrally mounted six-hole solenoid-actuated series production injector was employed, together with an intake stroke injection strategy to attain homogeneous operation. Moreover, the cylinder was equipped with a centrally mounted spark plug, and two piezoelectric transducers for the in-cylinder pressure measurement were oppositely mounted between the intake and exhaust valves. The intake and exhaust manifolds were fitted with pressure transducers as well. A hot-film air mass meter was used to measure the intake air mass flow, while a Coriolis-type mass flow sensor measured the fuel mass flow. To keep the imposed engine speed and load, the engine was coupled with an electric dynamometer and an eddy-current brake, respectively. To maintain the desired delta pressure between intake and exhaust, an external boosting system and an exhaust gas backpressure control valve were employed. For the exhaust gas components measurement (HC, CO, CO_2, NO_X, O_2), a partial exhaust gas mass flow was utilised to sample the species upstream of the backpressure control valve. Soot emissions were quantified by the filter smoke number (FSN) and measured downstream of the backpressure control valve. Eventually, HC emissions were measured as C_3H_8. A detailed description of all the measurement systems, with their respective measurement ranges and accuracies, is given in Table A.1 in the Appendix [33]. 200 cycles were recorded for each engine OP, and the mean quantities were used as input data for the present analysis.

As for the experimental data collection, the tested engine Operating Points (OP) for ethanol are reported in Table 3. Load variation tests were carried out at 2500 RPM from 3 up to 30 bar IMEP, and another engine OP was available at 2000 RPM, 12 bar IMEP. All the investigations were carried out at stoichiometric conditions.

Engine speed [1/min]	**IMEP [bar]**	**EGR [%]**	**Fuel**
2000	12	0	Ethanol
2500	3-30	0	Ethanol

Table 3. Investigated engine OP for ethanol

In the next section, the fuel combustion methodology will be presented together with the results coming from the three-pressure analysis.

Fuel combustion model methodology

Figure 1 highlights the methodology that was followed to carry out the analysis.

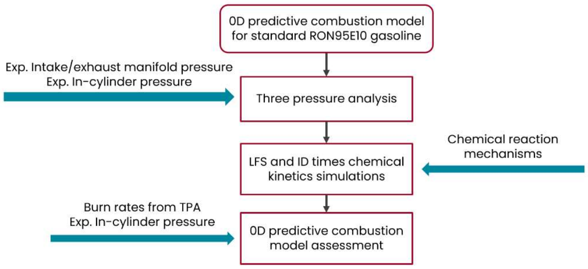

Figure 1. Activity workflow methodology

Starting from an existing 1D CFD model, representative of the single-cylinder research engine employed in this study, whose combustion model was previously calibrated for standard fossil gasoline, the experimental intake, exhaust manifold pressures and the in-cylinder one were used as inputs for the three-pressure analysis. This kind of simulation takes experimental boundary data like the in-cylinder pressure, the intake and exhaust port pressures (Figure 2), the valve lifts/timings, the tumble coefficients, the spark timing, the boundary intake and exhaust temperatures and the intake EGR fraction to estimate the in-cylinder conditions at intake valve closing (IVC). The dynamic profiles of the intake and exhaust manifold pressures, as well as the intake air temperature and EGR fraction, were imposed in the model by the “BoundaryPressureTPA” template. Other outputs of the TPA are the fuel burn rate and the simulated in-cylinder pressure when the estimated burn rate is imposed in the model. Those burn rate profiles will serve as the benchmark to which the predictive combustion model will be referenced for its performance assessment.

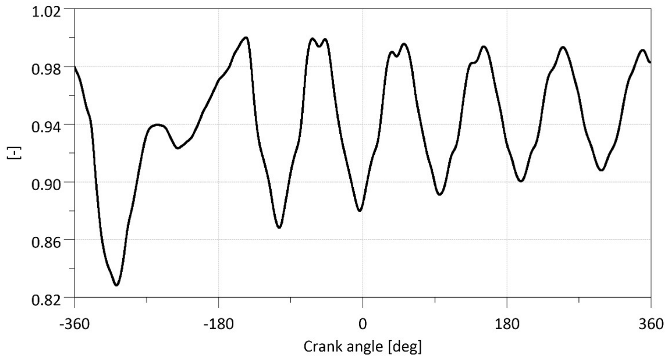

a) Normalised intake manifold pressure

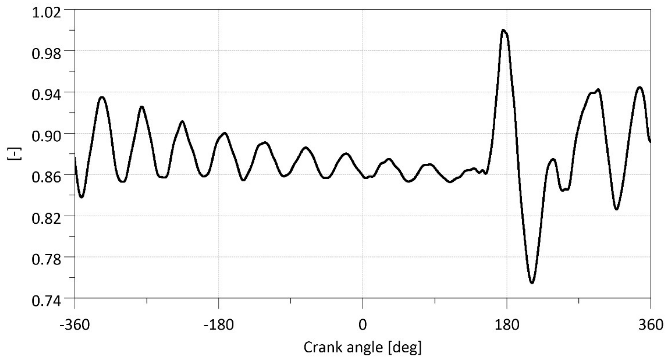

b) Normalised exhaust manifold pressures

Figure 2. Boundary intake and exhaust manifold pressures (2500 1/min, IMEP = 12 bar)

Subsequently, in order to customise the predictive combustion model fuel-wise, laminar flame speed and ignition delay times need to be estimated via chemical kinetics simulations. A proper grid of thermodynamic conditions, including the in-cylinder pressure, unburnt mixture temperature, the equivalence ratio and the EGR %, was given as input for chemical kinetics simulations together with the ethanol chemical composition. The results were then used to generate a custom LFS metamodel (neural network), which was integrated into the "EngCombSIturb" combustion model template. As for the ignition delays, a custom Python function was integrated into the model to interpolate at runtime the ID of the air-fuel mixture into the cylinder. The ID_s were employed to calculate the Livengood-Wu [40] induction time integral (ITI) to assess the knock occurrence. It is defined according to Eq. (1), where the Induction Time Multiplier (ITM) is used to tune the final integral value. If the integral at the end of the combustion phase overcomes a user-defined threshold (0.9 in this study), the simulated engine operating point is considered a knocking one. The threshold was reduced from 1 to 0.9 because the simulation results pertain to a mean cycle, and the combustion coefficient of variation (COV) is not modelled. On the contrary, if the COV is taken into account and the faster cycles are simulated, the knocking ITI threshold would be set to 1, meaning that the autoignition speed of the unburned gases is higher than the flame front propagation.

$$ITI = \int \frac{1}{\tau_{ID} * ITM} dt \qquad (1)$$

In the next section, the outcomes of each step of the aforementioned fuel combustion methodology will be analysed and discussed.

Results and discussions

Three pressure analysis

As previously mentioned, TPA is a crucial step in the analysis since, on one hand, it allows the validation of the experimental data acquisition and, on the other hand, it enables the possibility to estimate in-cylinder IVC conditions to subsequently perform the predictive combustion model assessment by a closed volume analysis. Consistency checks, mainly related to the LHV multiplier, have been addressed by adjusting the in-cylinder convection heat transfer multiplier. In addition, as for the fuel evaporation, an empirical correlation is considered in the model as shown in Eq. (2).

$$\frac{dm_{fuel_{evap}}}{dt} = \frac{1}{m_{fuel}} \left(4.16 * \frac{n_{ref}}{CA_{50,evap}}\right) \left(\frac{T}{T_{ref}}\right)^{T_{exp}} \left(\frac{T}{n_{ref}}\right)^{n_{exp}} \qquad (2)$$

This correlation is based on the idea that the engine speed and the in-cylinder temperature affect the evaporation rate of the injected fuel. As a matter of fact, as the engine speed increases, the in-cylinder flow motion gets more intense, enhancing the convective heat transfer between the spray droplets and the surrounding ambient. Similarly, as the in-cylinder temperature increases, more heat is transferred to the droplets, promoting evaporation. Three tuning parameters, T_{exp}, n_{exp} and $CA_{50,evap}$ can be adjusted to account for the influence of the temperature, engine speed and the evaporation duration. This last parameter is estimated at reference engine speed, n_{ref}, and temperature, T_{ref}. This approach is far from being predictive, but it allows to account for the effect of engine speed and load on the evaporation behaviour. Moreover, to account for possible fuel impingement on cylinder or piston walls, the heat subtracted from the evaporation process is assumed not to be entirely taken from the in-cylinder gas, but a part of it from the combustion chamber surfaces. The fraction of heat absorbed by the cylinder walls is parametrised in the model with $x_{heat,wall}$. As pointed out by Esposito et. al [41], this amount of heat subtracted from the walls has been shown to be crucial to match airflow and, so, engine performance. Considering the high heat of vaporisation of ethanol with respect to gasoline and its low AFR_s, the injection duration increases, likely resulting in more fuel impingement. Following the same approach of Esposito et. Al [41], an empirical correlation for $x_{heat,wall}$ was employed (Eq. (3)). In Table 4, the other evaporation parameters are reported along with the reference engine speed and temperature.

$$x_{heat,wall} = \max\left(c_{hw,0} - c_{hw,\lambda}\lambda - c_{hw,IMEP}IMEP, c_{hw,min}\right) \qquad (3)$$

Parameter	Value
n_{ref}	4000 1/min
T_{ref}	600 K
n_{exp}	1
T_{exp}	1
$CA_{50,evap}$	15
$c_{hw,0}$	1.032
$c_{hw,\lambda}$	0.34
$c_{hw,IMEP}$	0.005
$c_{hw,min}$	0.35

Table 4. Evaporation model parameters

Figure 3 depicts an example of the in-cylinder pressure coming from the TPA, along with the estimated burn rate profile, which best matches the experimental pressure curve. The simulated profile is obtained by imposing the estimated burn rate profile as the combustion model. The estimated burn rates will represent the reference profiles that the predictive combustion model should replicate.

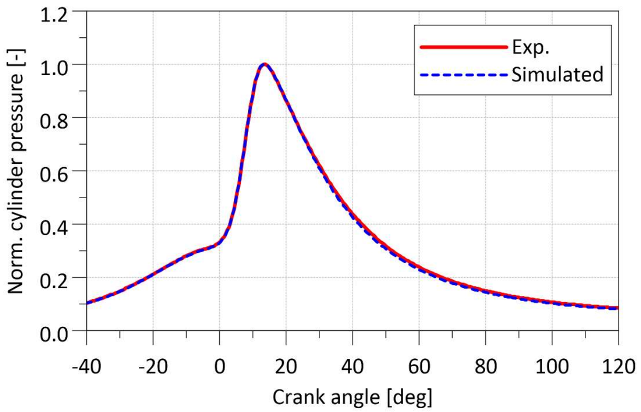

a. Normalised simulated and experimental in-cylinder pressure (2500 RPM, 12 bar IMEP, 0 % EGR)

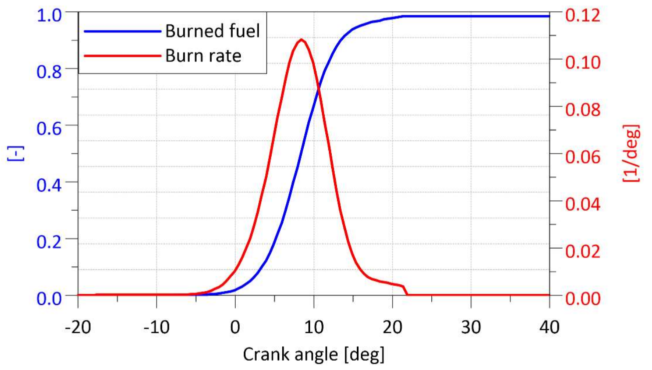

b. Reference burn rate profile (2500 RPM, 12 bar IMEP, 0 % EGR)

Figure 3. Three Pressure Analysis outcomes

Figure 4 illustrates the TPA outcomes in terms of Root Mean Square Error (RMSE), computed by comparing the simulated value with its experimental counterpart. The addressed metrics include Indicated Mean Effective Pressure (IMEP), Pumping Mean Effective Pressure (PMEP), maximum in-cylinder pressure, the crank angle at maximum pressure, the mixture mass fraction burned at 50% (MFB50), MFB1090, volumetric efficiency, the mass of air and fuel. As can be seen, all the addressed quantities are well reproduced by the TPA, underscoring the 1D CFD model's fidelity. As for the air mass, a higher deviation can be noticed, since the fuel flow rate is imposed in the model, while the mean intake manifold pressure is adjusted to meet the stoichiometric air-to-fuel ratio. Therefore, the air mass RMSE is higher. Anyway, if the mean percentage error is addressed, the air flow maximum deviation is below 2%.

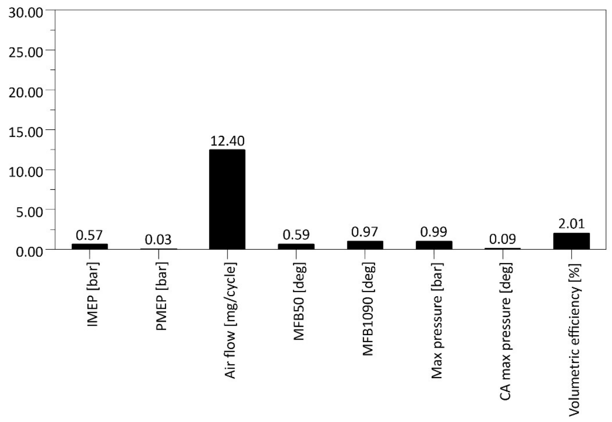

Figure 4. TPA Root Mean Square Error with respect to experimental data

Once reference burn rate profiles have been estimated, the next step is represented by the generation of fuel-specific laminar flame speed values to be then integrated into the predictive combustion model. In the following section, the methodology to achieve this end will be described and discussed.

Chemical kinetics simulations

Laminar flame speed neural network development

By following the approach of Del Pecchia et. al [42], the thermodynamic conditions to be used to perform chemical kinetics simulation for the LFS estimation were defined following a polytropic law, linking the unburnt mixture temperature, T_u, to the in-cylinder pressure, p_{cyl}. As shown in Figure 5, high-pressure and low-temperature grid points were not simulated, since it is unlikely that an engine will operate in such conditions. Moreover, the trend of the unburnt mixture temperature as a function of the in-cylinder pressure is reported from combustion onset to maximum cylinder pressure. As can be seen, the grid was properly conceived as all the curves are included in the grid. For ethanol, the employed chemical reaction mechanism [43] for the laminar flame speed simulations has just 67 species and 1016 reactions, enabling the possibility of designing a fine grid. The overall thermodynamic conditions, both for LFS neural network training and testing, are reported in Tables 5-6. The chemistry tool embedded in the Converge software was used to solve the chemical kinetics simulations [44].

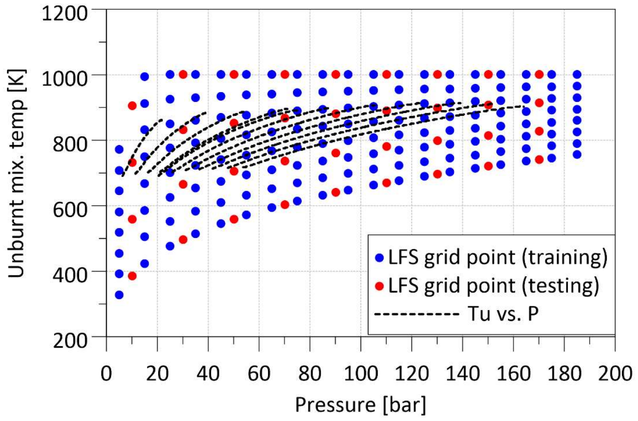

Figure 5. Ethanol LFS grid points for metamodel generation

	Pressure [bar]	Unburnt mix. T [K]	Equivalence ratio [-]	EGR [%]
Min	5	328	0.8	0
Max	185	1000	1.2	35
Delta	10	8 steps for each pressure value	0.1	5

Table 5 In-cylinder conditions for ethanol LFS training dataset

	Pressure [bar]	Unburnt mix. T [K]	Equivalence ratio [-]	EGR [%]
Min	10	385	0.9	2.5
Max	170	1000	1.1	27.5
Delta	20	4 steps for each pressure value	0.2	5

Table 6 In-cylinder conditions for ethanol LFS testing dataset

Once the laminar flame speed values were computed, the GT-Post metamodel generator tool was employed and fed with the computed LFS. The input features to train the network are the same as the ones used for the chemical kinetics simulations, and the output response is the LFS at that particular engine thermodynamic condition. A sweep of the most important hyperparameters was performed, such as the number of hidden layers, the number of neurons and the kind of hidden layer transfer functions, to choose the best neural network for predicting the testing LFS dataset. For the training, a cross-validation logic was employed using 20% of the training dataset for the network weights optimisation.

Figure 6 depicts the performance of the neural network featuring the highest coefficient of determination (R^2) and the lowest RMSE concerning the testing dataset.

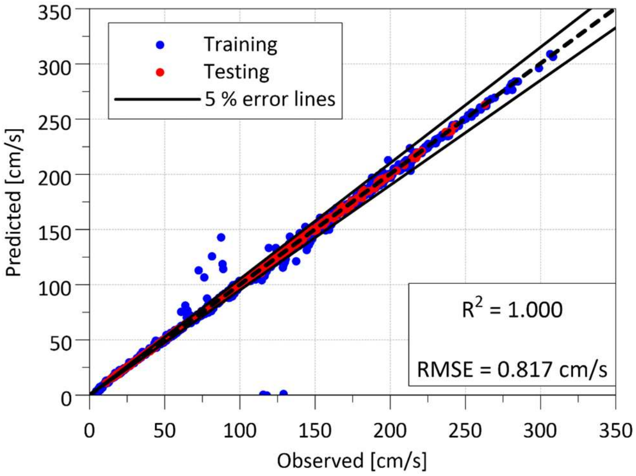

Figure 6. Ethanol LFS neural network performance

As can be seen, the neural network is able to replicate the testing dataset with excellent accuracy. This black-box model was then integrated into the combustion model for its prediction assessment.

The next section highlights the methodology employed to simulate the fuels' ignition delays in order to compute, during runtime, the Livengood-Wu knock induction time integral [40], enabling the possibility of assessing the knock phenomenon occurrence, as described in the Fuel Combustion Methodology Section.

Ignition delay simulations

In order to choose the best mechanism for replicating ethanol ignition delay, experimental ignition delay times were compared to 0D constant volume simulations, performed by employing the most commonly used chemical reaction mechanisms found in literature (Table 7).

Mechanism	Species	Reactions
LLNL [45]	1389	9603
LLNL reduced [45]	312	2469
Creck [46]	299	8028
Creck reduced [47]	156	3465
Andrae [48]	202	1010
ITV RWTH 2019 [49]	490	2081
C3MechV3 [50]	3761	16532
Aramco [51]	493	2716
NUIG High T. [52]	923	5966
ITV RWTH 2015 [53]	335	1613

Table 7 Investigated chemical reaction mechanism for ethanol ignition delays simulations

Table 8 sums up the thermodynamic conditions for which the selected chemical reaction mechanisms were evaluated. Chemical kinetics simulations were carried out in a 0D constant volume environment, with the use of Converge software [44]. Specifically, the auto-ignition time is defined as the time interval between the start of the simulation and the temperature rising by 400 K above the initial value.

Author	**Pressure [bar]**	**Unburnt mix. T [K]**	**Equivalence ratio [-]**
Nativel et. al [54]	20	800 - 1250	1
Zhang et. al [55]	20, 40	650 – 1200	0.5 – 2
Barraza-Botet et. al [56]	10	880 – 970	1
Cancino et. al [57]	10, 30, 50	650 – 1220	0.3, 1
Lee et. al [58]	35, 70, 80	750 – 1000	1
Barraza-Botet et. al [59]	3 – 10	880 – 1150	1

Table 8 Experimental ignition delay times thermodynamic conditions

In the present work, just the conditions corresponding to stoichiometric ones were addressed since all the engine OP$_s$ were investigated at $\phi = 1$.

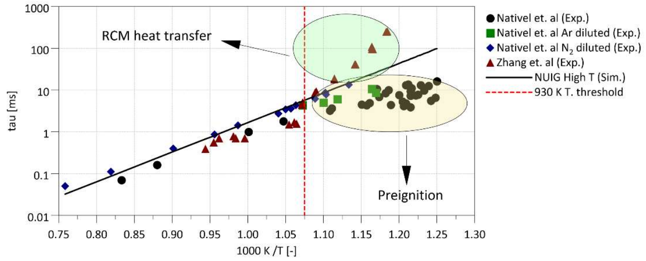

Figure 7 Ignition delay times comparison: (symbols) experimental, (line) simulations. Pressure = 20 bar, $\phi = 1$

The authors [54] suggested that for temperatures below 930 K, a large discrepancy between the closed volume simulations and the rapid compressor machine experimental results is observed. This is due to the heat transfer through the walls, which decreases the temperature inside the control system, increasing the experimental ignition delay time. Moreover, in the same work, it was acknowledged that for temperatures below 860 K, the ignition was not homogeneous in the shock tube control system. Local gas ignition was favouring the global mixture autoignition, thus lowering the ignition delay time. Therefore, in the present study, to evaluate the goodness of the chemical reaction mechanisms, only experimental ID$_s$ above 930 K were considered (Figure 7). The RMSE between the simulated and the experimental ID$_s$ was computed, and the best mechanism was selected for the knock assessment activity. In this case, the NUIG high T mechanism was best at reproducing experimental ethanol ignition delays data, showing the lowest RMSE (Figure 8).

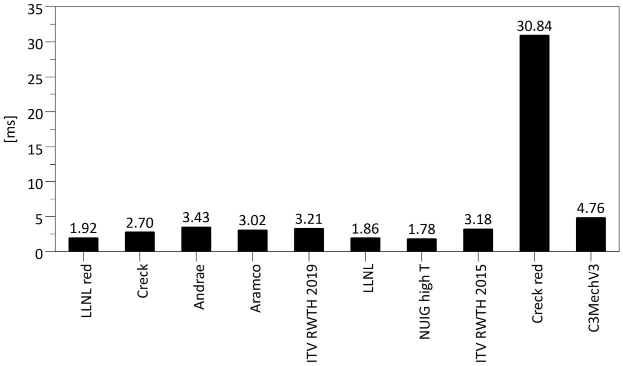

Figure 8 Chemical reaction mechanisms Root Mean Square Error with respect to experimental ethanol ignition delay data

The NUIG high T mechanism was then used to perform 0D closed volume ignition delays simulations according to Table 9, which reports the thermodynamic conditions employed to solve the chemical kinetics simulations. Here, the minimum temperature starts from 600 K, since for lower values the mixture autoignition occurs on a time scale far from one engine cycle duration.

	Pressure [bar]	**Unburnt mix. T [K]**	**Equivalence ratio [-]**	**EGR [%]**
Min	5	600	0.8	0
Max	185	1200	1.2	35
Delta	10	8 steps for each pressure value	0.1	5

Table 9 Ethanol constant volume ignition delays thermodynamic conditions

The ID grid was interpolated at runtime via a Python script, and the induction time integral was then computed by using Eq. (1). In the next section, the predictive combustion model performance will be assessed, along with the knock prediction model.

Combustion model assessment

In order to assess the performance of the predictive combustion model, closed-volume simulations were conducted starting from the in-cylinder IVC conditions estimated by the three-pressure analysis. As a remark, the combustion model was not recalibrated from the turbulent flame speed parameters point of view, but only the fuel laminar flame speed neural network was varied while switching from RON95E10 fuel to ethanol. In addition, the combustion model relies on a 0D in-cylinder turbulence model, previously calibrated by taking as reference data 3D CFD cold flow simulation results. The turbulent kinetic energy and integral length scale profiles were used to calibrate such a model, to reproduce the amount of turbulence level, which is a crucial input for the robustness of the combustion model. Moreover, the same spark timings coming from the engine test bench were used to set the combustion start in the model.

Figure 9 depicts the in-cylinder pressure curves and burned fuel fraction comparisons between the predictive combustion model and the reference profiles as the IMEP increases.

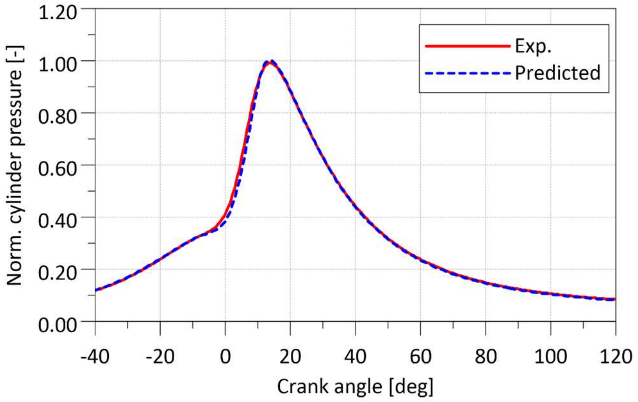

a. Ethanol in-cylinder pressure, 2500 RPM, 3 bar IMEP

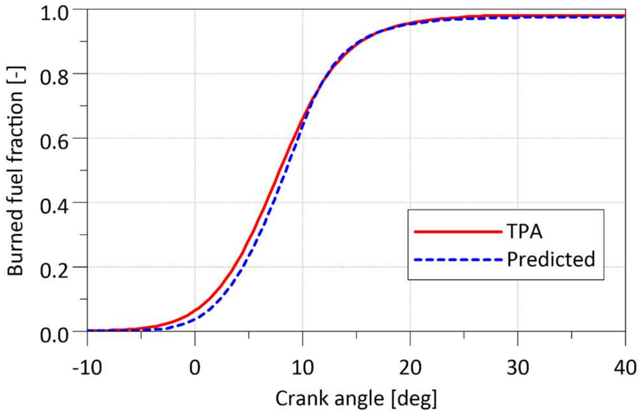

b. Ethanol burned fuel fraction, 2500 RPM, 3 bar IMEP

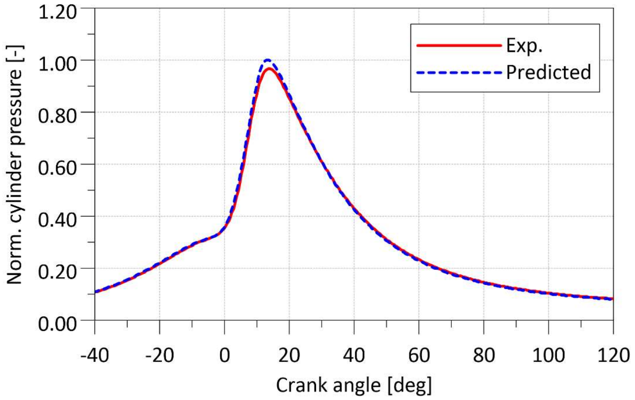

c. Ethanol in-cylinder pressure, 2500 RPM, 6 bar IMEP

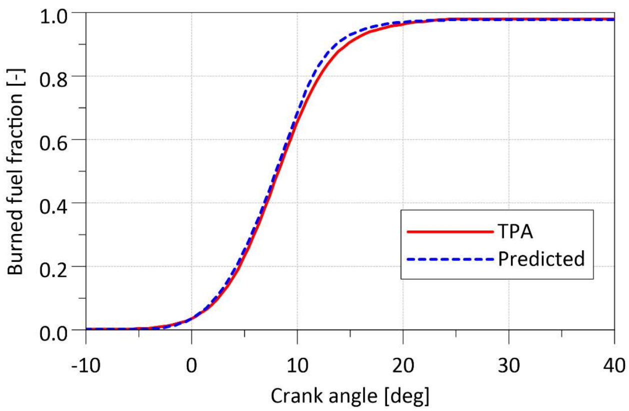

d. Ethanol burned fuel fraction, 2500 RPM, 6 bar IMEP

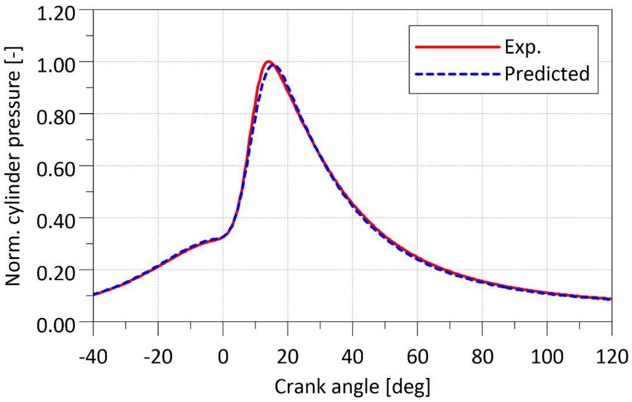

e. Ethanol in-cylinder pressure, 2500 RPM, 27 bar IMEP

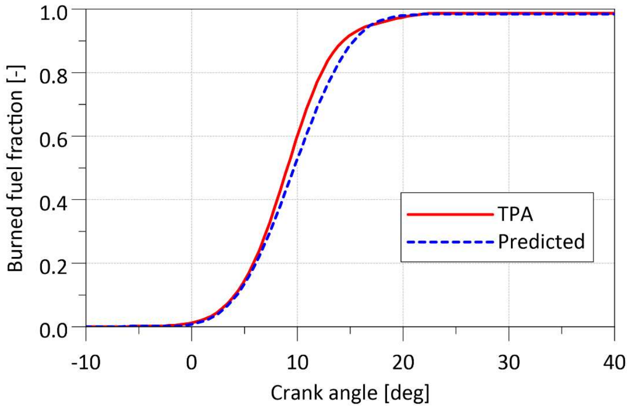

f. Ethanol burned fuel fraction, 2500 RPM, 27 bar IMEP

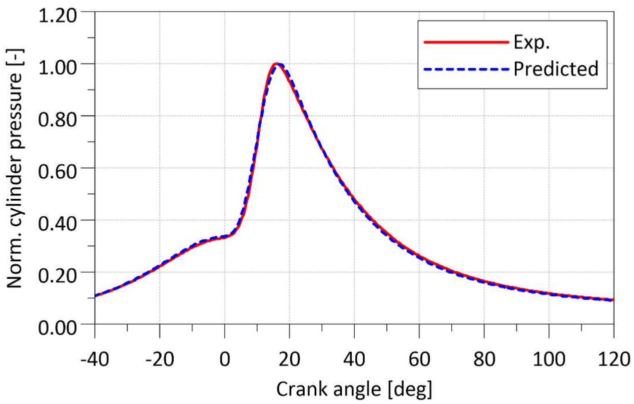

g. Ethanol in-cylinder pressure, 2500 RPM, 30 bar IMEP

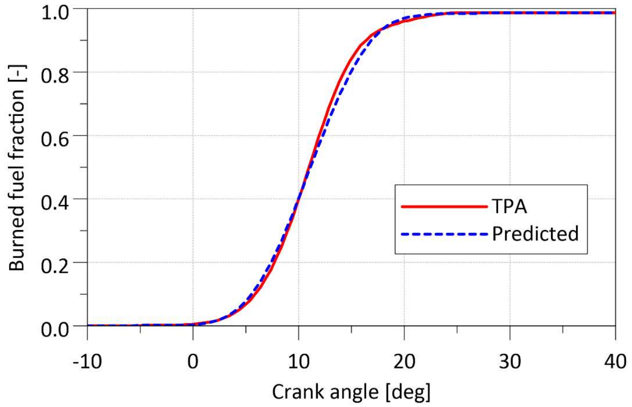

h. Ethanol burned fuel fraction, 2500 RPM, 30 bar IMEP

Figure 9. Predictive combustion model outcomes

From the plots, the predictive combustion model can predict the burn rate of the investigated fuel with high accuracy, for both low-load conditions (Figures 9a, 9b, 9c, 9d) and high ones (Figures 9e, 9f, 9g, 9h). In addition, by operating the SCRE with ethanol, the combustion phasing can always be maintained around the maximum efficiency even for very high IMEP. Owing to the ethanol knock resistance, the SA can be set in order to keep the MFB50 at the maximum combustion efficiency point without running into knock.

Combustion-related metrics were evaluated against the corresponding reference values coming from TPA. Specifically, the RMSE was used to assess the performance of the combustion model (Figure 10). As shown by the RMSE regarding MFB50 and MFB1090, the combustion phasing is overall captured, as well as the indicators regarding the cylinder pressure.

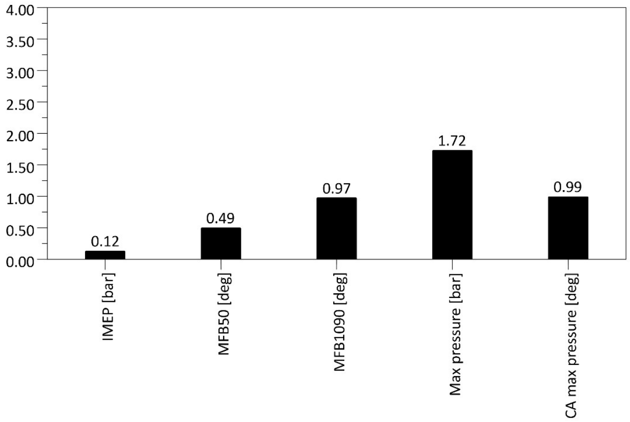

Figure 10. Predictive combustion model RMSE related to the main combustion metrics.

As a last analysis, in the following section, the knock prediction results, employing the induction time integral methodology, will be reported and discussed.

Knock prediction assessment

As mentioned in the Ignition Delay Simulations section, the simulated ignition delay grid was interpolated at runtime by employing a Python script, which was integrated into the 1D CFD SCRE model. The induction time integral (Eq. (1)) was then evaluated for each engine operating condition and compared with the normalised Mean Amplitude Pressure Oscillations (MAPO) 98.5 percentile (Eq. (4)). The knock limit is defined as in Eq. (5), and it includes the effect of the engine speed on the MAPO 98.5 percentile knock limit.

$$MAPO_{norm} = \frac{MAPO_{98.5}}{Knock\ limit} \tag{4}$$

$$Knock\ limit = \frac{RPM}{1000} + 0.5 \tag{5}$$

Knock is experimentally detected when the normalized $MAPO_{98.5}$ percentile value exceeds unity while, in the simulation, knock is identified when the ITI overcomes the 0.9 threshold. Figure 11 compares the ITI with the $MAPO_{norm}$.

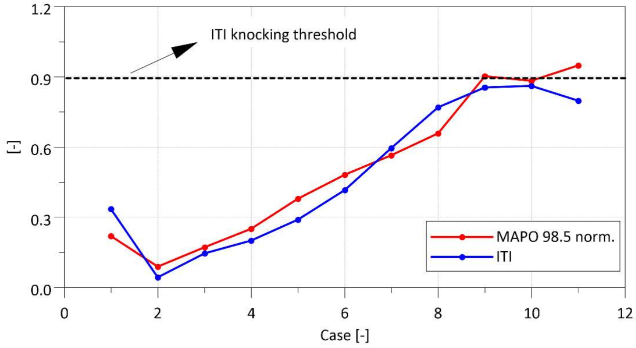

Figure 11. Ethanol knock induction time integral and normalised $MAPO_{98.5}$ percentile

In this work, to better align the normalised value of the $MAPO_{98.5}$ percentile to the induction time integral, the ITM was set to 0.55, which resulted in a higher value of the ITI at the end of combustion. This adjustment could be due to the uncertainty related to the fuel impingement on the cylinder walls, being the evaporation model a non-predictive one, and consequently, on the heat subtracted from the mixture. The great ethanol heat of vaporisation makes the fuel impingement prediction more sensitive to capture the right unburnt mixture temperature, a key variable for the mixture ignition delay. The ITM is meant to artificially correct such uncertainty to adapt the ITI to the experimental knock index.

From Figure 11, as the load increases from case 2 to 11, the ITI shows a growing trend, as the spark advance is kept attaining maximum combustion efficiency. Consequently, higher pressures and temperatures are achieved in the cylinder, and the probability of knock occurrence rises. The normalised $MAPO_{98.5}$ percentile does not overcome 1 even at 30 bar IMEP, highlighting the outstanding fuel knock resistance. As a matter of fact, by looking at the experimental pressure traces, high-frequency oscillations close to firing TDC, typical of knock occurrence, are not spotted (Figure 12). The value of the ITI for this last engine OP slightly reduces due to the fact that the SA is further retarded to comply with the knock limit. Anyway, the value of the $MAPO_{98.5}$ increases, meaning that such engine OP is really close to the knock limit, but the ITI seems not to capture the knock behaviour for this last operating condition. This could be caused by the slightly retarded combustion (Figure 9h and 13), from MFB60 to MFB90, which reduces the likelihood of knock occurrence with respect to the reference TPA burn rate profile.

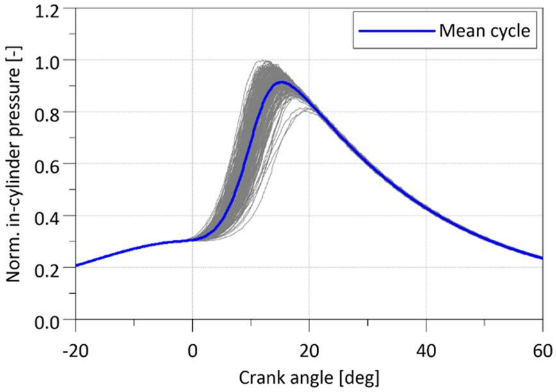

Figure 12. Ethanol experimental normalised pressure trace for the case at 30 bar IMEP, 2500 RPM, 0% EGR

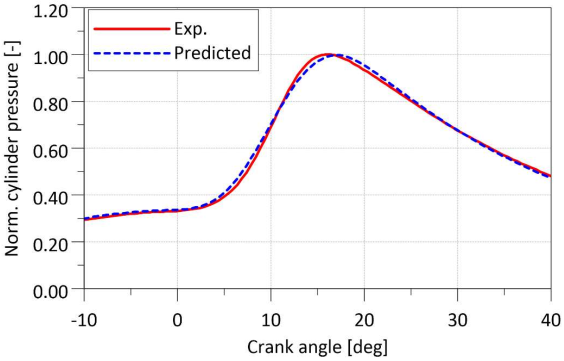

Figure 13. Case 11 zoomed in-cylinder pressure

Conclusions

This study focused on developing a fuel modelling methodology to extend an existing one-dimensional engine model – originally designed for fossil gasoline – to simulate combustion and knock dynamics of SI engines fuelled with ethanol. Fuel flexibility was achieved by integrating fuel-specific LFS and ID times into the model. The methodology was then validated using experimental data from an SCRE operated with ethanol.

To account for the dependency of LFS and ID on fuel composition, a grid of LFS and ID values, corresponding to different in-cylinder conditions, was generated for the fuel under analysis. The predictive combustion model was tailored according to the fuel by integrating an LFS neural network into the SI combustion template. The turbulent flame speed parameters were not recalibrated while switching fuel kinds.

Moreover, for the knock prediction, the Livengood-Wu knock induction time integral method was employed [40]. The predictive combustion is able to reproduce the experimental in-cylinder pressure, as well as the burn rate, with high accuracy. As for the knock model, the general trend of the normalised MAPO 98.5 percentile by the empirical knock limit is replicated by the model's ITI across various engine operating conditions. The overall methodology is proven to be adopted for multiple fuel kinds, enabling the possibility of simulating the combustion of a general gasoline-like fuel and reducing the need for experimental data acquisition.

The next application of such methodology will involve the use of synthetic e-gasoline fuels, in order to prove the robustness of such a process when applied to multi-component fuel mixtures.

References

[1] K. Calvin et al., 'IPCC, 2023: Climate Change 2023: Synthesis Report. Contribution of Working Groups I, II and III to the Sixth Assessment Report of the Intergovernmental Panel on Climate Change [Core Writing Team, H. Lee and J. Romero (eds.)]. IPCC, Geneva, Switzerland.', Intergovernmental Panel on Climate Change (IPCC), Jul. 2023. doi: 10.59327/IPCC/AR6-9789291691647.

[2] M. Bilgili, S. Tumse, and S. Nar, 'Comprehensive Overview on the Present State and Evolution of Global Warming, Climate Change, Greenhouse Gasses and Renewable Energy', Arab. J. Sci. Eng., vol. 49, no. 11, pp. 14503–14531, Nov. 2024, doi: 10.1007/s13369-024-09390-y.

[3] L. Pirjola et al., 'Potential of renewable fuel to reduce diesel exhaust particle emissions', Appl. Energy, vol. 254, p. 113636, Nov. 2019, doi: 10.1016/j.apenergy.2019.113636.

[4] L. Gren et al., 'Effects of renewable fuel and exhaust aftertreatment on primary and secondary emissions from a modern heavy-duty diesel engine', J. Aerosol Sci., vol. 156, p. 105781, Aug. 2021, doi: 10.1016/j.jaerosci.2021.105781.

[5] M. A. Ghadikolaei, 'Effect of alcohol blend and fumigation on regulated and unregulated emissions of IC engines—A review', Renew. Sustain. Energy Rev., vol. 57, pp. 1440–1495, May 2016, doi: 10.1016/j.rser.2015.12.128.

[6] G. Azhaganathan and A. Bragadeshwaran, 'Critical review on recent progress of ethanol fuelled flex-fuel engine characteristics', Int. J. Energy Res., vol. 46, no. 5, pp. 5646–5677, Apr. 2022, doi: 10.1002/er.7610.

[7] G. B. Machado et al., 'Investigations on surrogate fuels for high-octane oxygenated gasolines', Fuel, vol. 90, no. 2, pp. 640–646, Feb. 2011, doi: 10.1016/j.fuel.2010.10.024.

[8] Y. Kroyan, M. Wojcieszyk, O. Kaario, and M. Larmi, 'Modelling the end-use performance of alternative fuel properties in flex-fuel vehicles', Energy Convers. Manag., vol. 269, p. 116080, Oct. 2022, doi: 10.1016/j.enconman.2022.116080.

[9] M. Renzi, M. Bietresato, and F. Mazzetto, 'An experimental evaluation of the performance of a SI internal combustion engine for agricultural purposes fuelled with different bioethanol blends', Energy, vol. 115, pp. 1069–1080, Nov. 2016, doi: 10.1016/j.energy.2016.09.050.

[10] A. Z. Mendiburu et al., 'Ethanol as a renewable biofuel: Combustion characteristics and application in engines', Energy, vol. 257, p. 124688, Oct. 2022, doi: 10.1016/j.energy.2022.124688.

[11] G. Najafi, B. Ghobadian, T. Yusaf, S. M. Safieddin Ardebili, and R. Mamat, 'Optimization of performance and exhaust emission parameters of a SI (spark ignition) engine with gasoline–ethanol blended fuels using response surface methodology', Energy, vol. 90, pp. 1815–1829, Oct. 2015, doi: 10.1016/j.energy.2015.07.004.

[12] S. H. Park, J. Cha, H. J. Kim, and C. S. Lee, 'Effect of early injection strategy on spray atomization and emission reduction characteristics in bioethanol blended diesel fueled engine', Energy, vol. 39, no. 1, pp. 375–387, Mar. 2012, doi: 10.1016/j.energy.2011.12.050.

[13] A. C. T. Malaquias, N. A. D. Netto, F. A. R. Filho, R. B. R. Da Costa, M. Langeani, and J. G. C. Baêta, 'The misleading total replacement of internal combustion engines by electric motors and a study of the Brazilian ethanol importance for the sustainable future of mobility: a review', J. Braz. Soc. Mech. Sci. Eng., vol. 41, no. 12, p. 567, Dec. 2019, doi: 10.1007/s40430-019-2076-1.

[14] G. Kalghatgi, 'Is it really the end of internal combustion engines and petroleum in transport?', Appl. Energy, vol. 225, pp. 965–974, Sep. 2018, doi: 10.1016/j.apenergy.2018.05.076.

[15] R. D. Reitz et al., 'IJER editorial: The future of the internal combustion engine', Int. J. Engine Res., Sep. 2019, doi: 10.1177/1468087419877990.

[16] R. B. R. da Costa et al., 'Combustion, performance and emission analysis of a natural gas-hydrous ethanol dual-fuel spark ignition engine with internal exhaust gas recirculation', Energy Convers. Manag., vol. 195, pp. 1187–1198, Sep. 2019, doi: 10.1016/j.enconman.2019.05.094.

[17] R. B. R. da Costa, R. M. Valle, J. J. Hernández, A. C. T. Malaquias, C. J. R. Coronado, and F. J. P. Pujatti, 'Experimental investigation on the potential of biogas/ethanol dual-fuel spark-

ignition engine for power generation: Combustion, performance and pollutant emission analysis', Appl. Energy, vol. 261, p. 114438, Mar. 2020, doi: 10.1016/j.apenergy.2019.114438.

[18] S. Dong et al., 'Investigations on the effects of fuel stratification on auto-ignition and combustion process of an ethanol/diesel dual-fuel engine', Appl. Energy, vol. 230, pp. 19–30, Nov. 2018, doi: 10.1016/j.apenergy.2018.08.082.

[19] V. B. Pedrozo, I. May, W. Guan, and H. Zhao, 'High efficiency ethanol-diesel dual-fuel combustion: A comparison against conventional diesel combustion from low to full engine load', Fuel, vol. 230, pp. 440–451, Oct. 2018, doi: 10.1016/j.fuel.2018.05.034.

[20] V. B. Pedrozo and H. Zhao, 'Improvement in high load ethanol-diesel dual-fuel combustion by Miller cycle and charge air cooling', Appl. Energy, vol. 210, pp. 138–151, Jan. 2018, doi: 10.1016/j.apenergy.2017.10.092.

[21] K. Ahn, A. G. Stefanopoulou, and M. Jankovic, 'AFR-Based Fuel Ethanol Content Estimation in Flex-Fuel Engines Tolerant to MAF Sensor Drifts', IEEE Trans. Control Syst. Technol., vol. 21, no. 3, pp. 590–603, May 2013, doi: 10.1109/TCST.2012.2187786.

[22] T. C. C. de Melo et al., 'Hydrous ethanol–gasoline blends – Combustion and emission investigations on a Flex-Fuel engine', Fuel, vol. 97, pp. 796–804, Jul. 2012, doi: 10.1016/j.fuel.2012.03.018.

[23] A. K. Thakur, A. K. Kaviti, R. Mehra, and K. K. S. Mer, 'Progress in performance analysis of ethanol-gasoline blends on SI engine', Renew. Sustain. Energy Rev., vol. 69, pp. 324–340, Mar. 2017, doi: 10.1016/j.rser.2016.11.056.

[24] L. Bromberg, D. R. Cohn, and J. B. Heywood, 'Optimized fuel management system for direct injection ethanol enhancement of gasoline engines', US10619580B2, Apr. 14, 2020 Accessed: Apr. 01, 2025. [Online]. Available: https://patents.google.com/patent/US10619580B2/en

[25] R.-H. Chen, L.-B. Chiang, C.-N. Chen, and T.-H. Lin, 'Cold-start emissions of an SI engine using ethanol–gasoline blended fuel', Appl. Therm. Eng., vol. 31, no. 8, pp. 1463–1467, Jun. 2011, doi: 10.1016/j.applthermaleng.2011.01.021.

[26] T. Guo et al., 'A comparative experimental study on emission characteristics of a turbocharged gasoline direct-injection (TGDI) engine fuelled with gasoline/ethanol blends under transient cold-start and steady-state conditions', Fuel, vol. 277, p. 118153, Oct. 2020, doi: 10.1016/j.fuel.2020.118153.

[27] R. C. Costa and J. R. Sodré, 'Hydrous ethanol vs. gasoline-ethanol blend: Engine performance and emissions', Fuel, vol. 89, no. 2, pp. 287–293, Feb. 2010, doi: 10.1016/j.fuel.2009.06.017.

[28] K. Morganti, M. Almansour, A. Khan, G. Kalghatgi, and S. Przesmitzki, 'Leveraging the benefits of ethanol in advanced engine-fuel systems', Energy Convers. Manag., vol. 157, pp. 480–497, Feb. 2018, doi: 10.1016/j.enconman.2017.11.086.

[29] D. dos Santos Filho, A. P. Tschiptschin, and H. Goldenstein, 'Effects of ethanol content on cast iron cylinder wear in a flex-fuel internal combustion engine–A case study', Wear, vol. 406–407, pp. 105–117, Jul. 2018, doi: 10.1016/j.wear.2018.04.003.

[30] G. B. Machado, T. C. C. de Melo, and K. M. da Silva, 'GDI flex fuel engine: Influence of different fuels on the performance', Int. J. Engine Res., vol. 22, no. 11, pp. 3407–3414, Nov. 2021, doi: 10.1177/1468087420970357.

[31] G. B. Machado, T. C. C. de Melo, and A. C. de A. F. Candido, 'Flex-fuel engine: Influence of ethanol content on power and efficiencies', Int. J. Engine Res., vol. 22, no. 1, pp. 273–283, Jan. 2021, doi: 10.1177/1468087419833257.

[32] D. O. Marques, L. S. F. Trevizan, I. M. F. Oliveira, O. Seye, and R. E. P. Silva, 'Combustion assessment of an ethanol/gasoline flex-fuel engine', J. Braz. Soc. Mech. Sci. Eng., vol. 39, no. 4, pp. 1079–1086, Apr. 2017, doi: 10.1007/s40430-016-0609-4.

[33] C. Wouters et al., 'Evaluation of Synthetic Gasoline Fuels and Alcohol Blends in a Spark-Ignition Engine', SAE Int. J. Fuels Lubr., vol. 15, no. 3, pp. 04-15-03–0017, May 2022, doi: 10.4271/04-15-03-0017.

[34] J. W. G. Turner, A. Peck, and R. J. Pearson, 'Flex-Fuel Vehicle Development to Promote Synthetic Alcohols as the Basis of a Potential Negative-CO2 Energy Economy', SAE International, Warrendale, PA, SAE Technical Paper 2007-01–3618, Aug. 2007. doi: 10.4271/2007-01-3618.

[35] A. S. O. Yu, P. T. de Souza Nascimento, F. E. B. Nigro, B. W. B. Frederick, W. G. Junior, and K. G. P. C. de Mello, 'Supplier involvement in flex-fuel technology development: The general motors and Volkswagen Brazilian cases', in PICMET '09 - 2009 Portland International Conference on Management of Engineering & Technology, Aug. 2009, pp. 1616–1625. doi: 10.1109/PICMET.2009.5261960.

[36] J. C. Keck, J. B. Heywood, and G. Noske, 'Early Flame Development and Burning Rates in Spark Ignition Engines and Their Cyclic Variability', SAE International, Warrendale, PA, SAE Technical Paper 870164, Feb. 1987. doi: 10.4271/870164.

[37] T. Morel et al., 'Model for Heat Transfer and Combustion In Spark Ignited Engines and its Comparison with Experiments', presented at the SAE International Congress and Exposition, SAE International, Feb. 1988. doi: 10.4271/880198.

[38] M. Metghalchi and J. C. Keck, 'Burning velocities of mixtures of air with methanol, isooctane, and indolene at high pressure and temperature', Combust. Flame, vol. 48, pp. 191–210, Jan. 1982, doi: 10.1016/0010-2180(82)90127-4.

[39] Ö. L. Gülder, 'Correlations of Laminar Combustion Data for Alternative S.I. Engine Fuels', SAE International, Warrendale, PA, SAE Technical Paper 841000, Aug. 1984. doi: 10.4271/841000.

[40] J. C. Livengood and P. C. Wu, 'Correlation of autoignition phenomena in internal combustion engines and rapid compression machines', Symp. Int. Combust., vol. 5, no. 1, pp. 347–356, Jan. 1955, doi: 10.1016/S0082-0784(55)80047-1.

[41] S. Esposito et al., 'Methanol fuelling of a spark-ignition engine: Experiments and 0D/1D predictive modelling for combustion,

performance, and emissions’, Fuel, vol. 393, p. 134657, Aug. 2025, doi: 10.1016/j.fuel.2025.134657.

[42] M. Del Pecchia, V. Pessina, F. Berni, A. d’Adamo, and S. Fontanesi, ‘Gasoline-ethanol blend formulation to mimic laminar flame speed and auto-ignition quality in automotive engines’, Fuel, vol. 264, p. 116741, Mar. 2020, doi: 10.1016/j.fuel.2019.116741.

[43] S. Roy and O. Askari, ‘A New Detailed Ethanol Kinetic Mechanism at Engine-Relevant Conditions’, Energy Fuels, vol. 34, no. 3, pp. 3691–3708, Mar. 2020, doi: 10.1021/acs.energyfuels.9b03314.

[44] ‘Richards, K.J., Senecal, P.K., and Pomraning, E., CONVERGE 4.1, Convergent Science, Madison, WI (2025).’

[45] M. Mehl, W. J. Pitz, C. K. Westbrook, and H. J. Curran, ‘Kinetic modeling of gasoline surrogate components and mixtures under engine conditions’, Proc. Combust. Inst., vol. 33, no. 1, pp. 193–200, Jan. 2011, doi: 10.1016/j.proci.2010.05.027.

[46] ‘CRECK_2003_TPRF_HT_ALC_NOX - Creckmodeling’. Accessed: Sep. 24, 2024. [Online]. Available: https://creckmodeling.chem.polimi.it/menu-kinetics/menu-kinetics-detailed-mechanisms/107-category-kinetic-mechanisms/414-mechanisms-1911-tprf-ht-alc-nox/

[47] E. Ranzi, A. Frassoldati, A. Stagni, M. Pelucchi, A. Cuoci, and T. Faravelli, ‘Reduced Kinetic Schemes of Complex Reaction Systems: Fossil and Biomass-Derived Transportation Fuels’, Int. J. Chem. Kinet., vol. 46, no. 9, pp. 512–542, Sep. 2014, doi: 10.1002/kin.20867.

[48] J. C. G. Andrae, ‘Comprehensive chemical kinetic modeling of toluene reference fuels oxidation’, Fuel, vol. 107, pp. 740–748, May 2013, doi: 10.1016/j.fuel.2013.01.070.

[49] L. Cai, A. Ramalingam, H. Minwegen, K. Alexander Heufer, and H. Pitsch, ‘Impact of exhaust gas recirculation on ignition delay times of gasoline fuel: An experimental and modeling study’, Proc. Combust. Inst., vol. 37, no. 1, pp. 639–647, 2019, doi: 10.1016/j.proci.2018.05.032.

[50] S. Dong et al., ‘A new detailed kinetic model for surrogate fuels: C3MechV3.3’, Appl. Energy Combust. Sci., vol. 9, p. 100043, Mar. 2022, doi: 10.1016/j.jaecs.2021.100043.

[51] Y. Li, C.-W. Zhou, K. P. Somers, K. Zhang, and H. J. Curran, ‘The oxidation of 2-butene: A high pressure ignition delay, kinetic modeling study and reactivity comparison with isobutene and 1-butene’, Proc. Combust. Inst., vol. 36, no. 1, Art. no. 1, Jan. 2017, doi: 10.1016/j.proci.2016.05.052.

[52] Y. Wu et al., ‘Understanding the antagonistic effect of methanol as a component in surrogate fuel models: A case study of methanol/n-heptane mixtures’, Combust. Flame, vol. 226, pp. 229–242, Apr. 2021, doi: 10.1016/j.combustflame.2020.12.006.

[53] L. Cai and H. Pitsch, ‘Optimized chemical mechanism for combustion of gasoline surrogate fuels’, Combust. Flame, vol. 162, no. 5, pp. 1623–1637, May 2015, doi: 10.1016/j.combustflame.2014.11.018.

[54] D. Nativel, P. Niegemann, J. Herzler, M. Fikri, and C. Schulz, ‘Ethanol ignition in a high-pressure shock tube: Ignition delay time and high-repetition-rate imaging measurements’, Proc. Combust. Inst., vol. 38, no. 1, pp. 901–909, 2021, doi: 10.1016/j.proci.2020.07.021.

[55] Y. Zhang, H. El-Merhubi, B. Lefort, L. Le Moyne, H. J. Curran, and A. Kéromnès, ‘Probing the low-temperature chemistry of ethanol via the addition of dimethyl ether’, Combust. Flame, vol. 190, pp. 74–86, Apr. 2018, doi: 10.1016/j.combustflame.2017.11.011.

[56] C. L. Barraza-Botet, J. Luecke, B. T. Zigler, and M. S. Wooldridge, ‘The impact of physicochemical property interactions of iso-octane/ethanol blends on ignition timescales’, Fuel, vol. 224, pp. 401–411, Jul. 2018, doi: 10.1016/j.fuel.2018.03.105.

[57] L. R. Cancino, M. Fikri, A. A. M. Oliveira, and C. Schulz, ‘Measurement and Chemical Kinetics Modeling of Shock-Induced Ignition of Ethanol−Air Mixtures’, Energy Fuels, vol. 24, no. 5, pp. 2830–2840, May 2010, doi: 10.1021/ef100076w.

[58] C. Lee et al., ‘On the Chemical Kinetics of Ethanol Oxidation: Shock Tube, Rapid Compression Machine and Detailed Modeling Study’, Z. Für Phys. Chem., vol. 226, no. 1, pp. 1–28, Jan. 2012, doi: 10.1524/zpch.2012.0185.

[59] C. L. Barraza-Botet, S. W. Wagnon, and M. S. Wooldridge, ‘Combustion Chemistry of Ethanol: Ignition and Speciation Studies in a Rapid Compression Facility’, J. Phys. Chem. A, vol. 120, no. 38, pp. 7408–7418, Sep. 2016, doi: 10.1021/acs.jpca.6b06725.

Corresponding author:

Eng. Lorenzo Ferrari
University of Bologna
Email: lorenzo.ferrari28@unibo.it

Definitions/Abbreviations

0D/1D/3D	Zero/One/Three Dimensional
AFR$_s$	Stoichiometric Air-to-Fuel Ratio
BMEP	Brake Mean Effective Pressure
CA	Crank Angle
CI	Compression Ignited
CFD	Computational Fluid Dynamics

COV	Coefficient of Variation
CR	Compression Ratio
C_3H_8	Propane
CO	Carbon Monoxide
CO_2	Carbon Dioxide
EGR	Exhaust Gas Recirculation
EMS	Engine Management System
FFV	Flex Fuel Vehicles
FSN	Filter Smoke Number
GHG_s	Greenhouse Gases
HC	Unburnt Hydrocarbons
ICE	Internal Combustion Engine
ID	Ignition Delay
IMEP	Indicated Mean Effective Pressure
ITI	Induction Time Integral
ITM	Induction Time Multiplier
IVC	Intake Valve Closing
LFS	Laminar Flame Speed
LHV	Lower Heating Value
MAPO	Mean Amplitude Pressure Oscillation
MBT	Maximum Brake Torque
MFB50	Angle of 50% Mass Fraction Burned
MFB1090	Angle Interval Between 10% and 90% Mass Fraction Burned
MON	Motor Octane Number
MtG	Methanol-To-Gasoline
NOx	Nitrogen Oxides
O_2	Oxygen
OP	Operating Point
PMEP	Pumping Mean Effective Pressure
RCM	Rapid Compression Machine
RMSE	Root Mean Square Error
RON	Research Octane Number
RPM	Revolutions Per Minute
SCRE	Single-Cylinder Research Engine
SI	Spark Ignited
TDC	Top Dead Center
TPA	Three Pressure Analysis
VVT	Variable Valve Timing
VO	Oxygenated Volume Fraction

Symbols

$c_{hw,0}$	Constant parameter for evaporation model
$c_{hw,\lambda}$	Lambda dependent parameter for evaporation model
$c_{hw,IMEP}$	IMEP dependent parameter for evaporation model
$c_{hw,min}$	Constant minimum parameter for evaporation model
$CA_{50,evap}$	Crank angle at 50 % fuel evaporation
λ	Normalised Air-To-Fuel Ratio (Lambda)
$m_{fuel,evap}$	Evaporated fuel mass
m_{fuel}	Injected fuel mass
n_{exp}	Engine speed exponent for evaporation model
n_{ref}	Reference engine speed for evaporation model
p_{cyl}	In-cylinder Pressure

$\boldsymbol{R^2}$	Coefficient of Determination
$\boldsymbol{\tau_{ID}}$	Ignition Delay
$\boldsymbol{T_{exp}}$	Temperature exponent for evaporation model
$\boldsymbol{T_{ref}}$	Reference temperature for evaporation model
$\boldsymbol{T_u}$	Unburnt Mixture Temperature
$\boldsymbol{x_{heat,wall}}$	Fraction of evaporation heat subtracted from cylinder walls

Appendix

Table A.1 Specifications of the test cell measurement instruments [33]

Instrument	Model	Measurement range	Accuracy
Engine dynamometer	Schorch	0-10,000 1/min	≤ 0.04 %
Air mass flow meter	FEV air rate	0-1000 kg/h	≤ 1.00 %
Fuel mass flow meter	Emerson Micro Motion Coriolis CMFS007	0-34.92 kg/h	≤ 0.054 %
In-cylinder pressure transducers	Kistler 6044A	0-300 bar	≤ 0.13 % at 30 bar ≤ 0.01 % at 200 bar
Intake pressure transducers	Kistler 4045A	0-5 bar	≤ 0.3 %
Exhaust pressure transducers	Kistler 4045A	0-5 bar	≤ 0.3 %
Exhaust gas analyser			
CLD (NO_X)	Eco Physics nCLD 811 M	0-5000 ppm	≤ 1 %
NDIR (CO, CO_2)	Rosemount NGA 2000	0-10 % (CO) 0-20 % (CO_2)	≤ 1 %
PMD (O_2)	Rosemount NGA 2000	0-25 %	≤ 1 %
FID (HC)	Rosemount NGA 2000	10-10,000 ppm	≤ 1 %
Particulate matter, soot	AVL 415SE smoke meter	0-10 FSN	0.0001 FSN

CLD = chemiluminescence detector, NDIR = non-dispersive infrared detector, PMD = paramagnetic detector, FID = flame ionization detector, THC = total-HC referred to propane (C3), FSN = filter smoke number.